Naval Research Laboratory
Washington, DC 20375-5320

NRL/6390/MR—2022/2

Accurate Computation of Excitons in Two-Dimensional Semiconducting Transition Metal Dichalcogenides

MADELEINE PHILLIPS

Materials Physics and Technology Branch
Materials Science and Technology Division

March 21, 2022

REPORT DOCUMENTATION PAGE

Form Approved
OMB No. 0704-0188

1. REPORT DATE *(DD-MM-YYYY)*	**2. REPORT TYPE**	**3. DATES COVERED** *(From - To)*
21-03-2022	NRL Memorandum Report	19 Jan 2021 – 18 Jan 2022

4. TITLE AND SUBTITLE

Accurate Computation of Excitons in Two-Dimensional Semiconducting Transition Metal Dichalcogenides

5a. CONTRACT NUMBER

5b. GRANT NUMBER

5c. PROGRAM ELEMENT NUMBER
NISE

6. AUTHOR(S)

Madeleine Phillips

5d. PROJECT NUMBER

5e. TASK NUMBER

5f. WORK UNIT NUMBER
N2Z6

7. PERFORMING ORGANIZATION NAME(S) AND ADDRESS(ES)

Naval Research Laboratory
4555 Overlook Avenue, SW
Washington, DC 20375-5320

8. PERFORMING ORGANIZATION REPORT NUMBER

NRL/6390/MR--2022/2

9. SPONSORING / MONITORING AGENCY NAME(S) AND ADDRESS(ES)

Naval Research Laboratory
4555 Overlook Avenue, SW
Washington, DC 20375-5320

10. SPONSOR / MONITOR'S ACRONYM(S)

NRL-NISE

11. SPONSOR / MONITOR'S REPORT NUMBER(S)

12. DISTRIBUTION / AVAILABILITY STATEMENT

DISTRIBUTION STATEMENT A: Approved for public release; distribution is unlimited.

13. SUPPLEMENTARY NOTES

*Karles Fellowship

14. ABSTRACT

This report presents research conducted by Madeleine Phillips under a Karles Fellowship over the period January 2021 through January 2022. The optoelectronic response of two-dimensional semiconducting transition metal dichalcogenides (TMDs) is dominated by excitons, which are bound states of electrons and holes. The excitonic spectrum of 2D TMDs can be manipulated by stacking TMDs or by stacking and introducing an interlayer twist. This report focuses on the variation of excitonic properties in WSe2 bilayers with two distinct twist angles: 0 and 60 degrees. These bilayers are often referred to as having 3R and 2H stacking, respectively. This work was published in part in the journal Nanoscale in January 2022.

15. SUBJECT TERMS

Density functional theory
2D materials
Model hamiltonians
Excitons

16. SECURITY CLASSIFICATION OF:			**17. LIMITATION OF ABSTRACT**	**18. NUMBER OF PAGES**	**19a. NAME OF RESPONSIBLE PERSON**
					Madeleine Phillips
a. REPORT	**b. ABSTRACT**	**c. THIS PAGE**	U	16	**19b. TELEPHONE NUMBER** *(include area code)*
U	U	U			(202) 767-6990

Standard Form 298 (Rev. 8-98)
Prescribed by ANSI Std. Z39.18

This page intentionally left blank.

CONTENTS

This page intentionally left blank.

EXECUTIVE SUMMARY

This report presents research conducted by Madeleine Phillips under a Karles Fellowship over the period January 2021 through January 2022. The optoelectronic response of two-dimensional semiconducting transition metal dichalcogenides (TMDs) is dominated by excitons, which are bound states of electrons and holes. The excitonic spectrum of 2D TMDs can be manipulated by stacking TMDs or by stacking and introducing an interlayer twist. Over the course of this Karles Fellowship, several systems were studied, including a WSe_2/WS_2 heterobilayer, a WSe_2/Bi_2Se_3 heterostructure, and a twisted $MoSe_2/WSe_2$ system, all of which have interesting excitonic features. This report focuses on the variation of excitonic properties in WSe_2 bilayers with two distinct twist angles: 0 and 60 degrees. These bilayers are often referred to as having 3R and 2H stacking, respectively. This work was published in part in the journal *Nanoscale* in January 2022.

This page intentionally left blank.

ACCURATE COMPUTATION OF EXCITONS IN TWO-DIMENSIONAL SEMICONDUCTING TRANSITION METAL DICHALCOGENIDES

INTRODUCTION

Background

The field devoted to the study of atomically thin or few-atom thick layers of crystalline material (so-called "two-dimensional materials") emerged in 2004 with the isolation of atomically thin graphite, known as "graphene" [1]. Since then, a dizzying variety of 2D materials have been isolated, from 2D insulators like hexagonal boron nitride (hBN), to 2D magnets like chromium iodide (CrI3), to 2D semiconductors like tungsten diselenide (WSe_2) [2, 3]. 2D materials are attractive from an application standpoint for a number of reasons: first they are essentially all surface, making them very sensitive to their environment and thus good candidates for sensing technologies [4]. Second, because of their incredibly limited size in one direction, devices made from 2D materials can be light-weight and operate at low-power, making them especially attractive for use in naval scenarios, where accessible space and power are both limited.

The semiconducting 2D materials made of three-atom-thick layers of transition metal dichalcogenides (TMDs) are particularly interesting for electronic device applications because they have an energy band gap in the visible light range, meaning one can couple to their electronic states not only using electric current but also using light. Furthermore, their optical response in the visible range is dominated by tightly-bound excitons, which are bound states made up of electrons and holes [5]. It is essential to understand the excitonic physics in 2D TMDs in order to understand and manipulate their optoelectronic response for optimal device design.

The primary excitonic transitions in a generic TMD monolayer (i.e. one formula unit, or three atoms, thick) are illustrated schematically in Figure 1. The primary band gap in the material is at the valley at the K point in the Brillouin zone, where both the conduction and valence bands are split by spin-orbit coupling and the resulting bands are spin-polarized. There are two primary transitions at the K point: the A and the B exciton. Optical selection rules in this material dictate that the electron and hole that make up the exciton bound state must originate from bands of the same spin [5]. Here the A exciton originates from the spin-down bands and the higher energy B exciton from the spin-up bands. The spins associated with the A and B excitons will be reversed at the K' (-K) valley. The spin-polarization of the excitons allows the valleys to be selectively addressable with circularly polarized light, another avenue for technological application [5]. The final transition shown in Figure 1 is an indirect excitonic transition associated with a hole at the K valley and an electron in the Q valley, which is situated on the K to Γ line in momentum space. Indirect excitons are currently less well characterized than their direct counterparts [6].

Manuscript approved February 22, 2022.

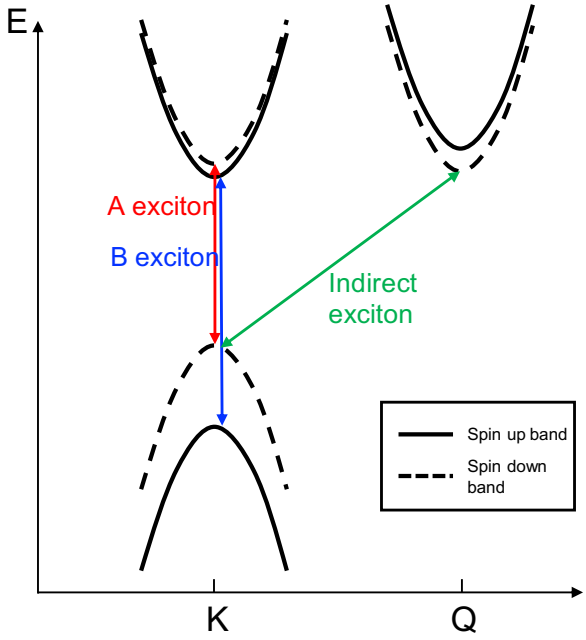

Figure 1 – Schematic of exciton transitions in a generic TMD monolayer. In TMDs, the hole and electron involved in an excitonic transition must originate from bands of the same spin.

The field of 2D materials study is almost twenty years old, and there are many aspects of atomically thin materials that have been well-characterized [2]. However, in 2018 it was discovered that stacking and twisting two or more monolayers can result in a multi-layer whose properties are significantly altered with respect to the constituent monolayers [7] or to other twist angles. Essentially, the twist angle between two monolayers is a recently-discovered "knob" for tuning the physics of 2D materials [8]. This discovery has required that new efforts be made to understand the effect of twist on materials properties, including excitonic properties, in the pursuit of making yet-further customizable devices.

In this report, we focus on the study of bilayer WSe_2, comparing the excitons in 0 degree and 60 degree twisted samples (Figure 2). The thermodynamically favorable stackings at these angles are often referred to as "3R" and "2H" stacking, respectively, since layers arranged at these highly commensurate twist angles are the building blocks of bulk TMDs designated as "3R" or "2H" [9]. This material is particularly suited to theoretical study, since it can be addressed in first-principles calculations with small unit cell sizes, due to the commensurate nature of the stacking. Furthermore, the symmetries of this system make it tractable for addressing with analytical Hamiltonians. The 2H (60 degree twisted) bilayer has inversion symmetry—that is, the system remains unchanged if the coordinate of each atom undergoes the transformation (x, y, z) → (-x, -y, -z). The 3R system exists in two polytypes: AB and BA (see Figure 2e). These two structures are inversion partners, so if the atoms in the AB structure undergo the transformation (x, y, z) → (-x, -y, -z), the BA structure results.

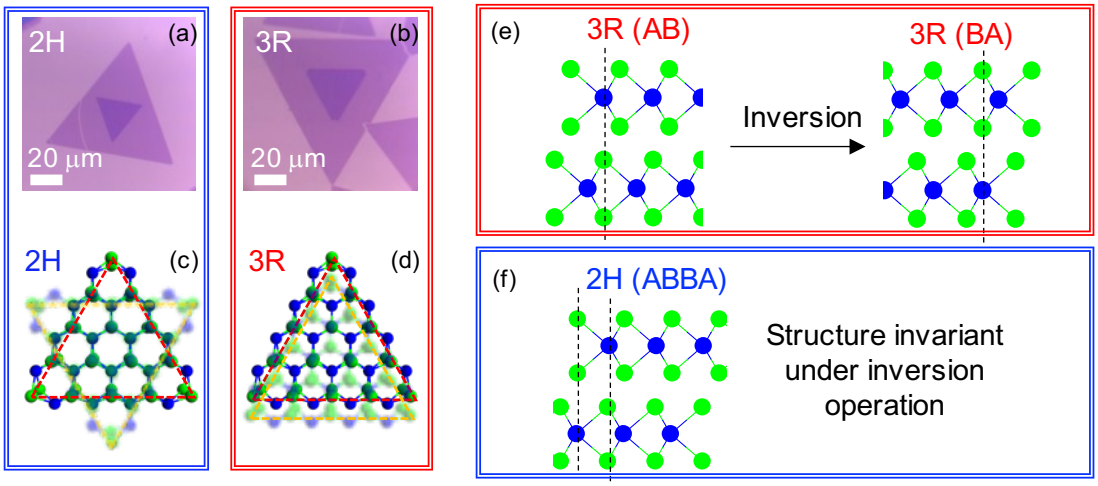

Figure 2 – Structure of 2H and 3R WSe_2 bilayers. (a, b) Optical images of 2H and 3R WSe_2 bilayer samples, respectively. (c, d) Schematics of the 2H and 3R structures, viewed from the top down. Green atoms are selenium, and blue atoms are tungsten. (e, f) Side views of the 3R and 2H structures. Note that there are two thermodynamically equivalent 3R structures, AB and BA, which are related by an inversion operation. The 2H structure (ABBA) is its own inversion partner. Figure adapted from reference [9].

Project Goals

The goal of this project is to show that theoretical methods such as Density Functional Theory and analytic Hamiltonian modeling can accurately capture important elements of exciton physics in 2D materials with different twist angles. In particular, we aim to understand and compare the excitons in 3R WSe_2 bilayers with those in 2H WSe_2 bilayers. The understanding we glean from this study can provide the foundation for device design utilizing excitonic features of highly-tunable twisted two-dimensional materials.

APPROACH

Density Functional Theory (DFT)

Our primary approach to studying the excitonic physics of WSe_2 homobilayers is to compute and compare the interband transitions associated with each exciton using Density Functional Theory (DFT). DFT is a type of first-principles method for solving the Schrodinger equation using electron densities, which reduces the computational resources necessary. We compute band structures for both the 2H and 3R WSe_2 bilayers and compare the interband transitions associated with A and B excitons in each structure.

We use the generalized gradient approximation of Perdew-Burke-Ernzerhof (PBE) [10] and the projected augmented wave (PAW) approach [11,12] as implemented in the Vienna Ab-initio Simulation Package (VASP) [13]. We add a van der Waals correction using the DFT-D3 method of Grimme [14]. We use a k-point grid of at least 8x8x1 points and an energy cutoff of 450 eV. Calculations are converged to within $1x10^{-8}$ eV. Spin orbit interactions are included in electronic calculations. The tungsten potential we use includes 14 valence electrons, and the selenium potential we use includes 6 valence electrons.

DFT within the PBE framework has limitations regarding the accuracy of the band gaps computed: in fact, it is known that such calculations systematically underestimate band gaps [15]. They also do not capture electron-electron interactions, which are necessary to obtain a quantitative value for the binding

energy of an exciton. However, PBE calculations are good candidates when one aims to compare similar structures with the same atomic make-up, as we do here. In this case, the underestimation of the band gap is expected to be the same for the WSe_2 bilayers in different stacking configurations, so if one studies the *difference* in band gaps, the DFT-induced error cancels out. Similarly, the exciton binding energies for bound states in 3R and 2H WSe_2 bilayers are expected to be very similar, and so this binding energy is expected to cancel out when taking differences in excitonic energies across the two systems. As we shall see, the results from a comparison of our DFT band structures agrees well with experimental data, supporting the claim that PBE DFT calculations are useful for comparing similar structures.

Analytic Hamiltonians

An important piece of knowledge to have when analyzing excitonic physics using band structures is the layer and spin character of each band. As described in the introduction, in TMDs, optical selection rules dictate that the electron and hole involved in each excitonic transition must have the same spin [5]. In bilayers, they must also originate in the same layer. For carriers with canted spins or which are delocalized between layers, there must be at least some overlap in layer and spin for a bright transition to occur.

The layer and spin character of the bands in the 3R bilayer structures (AB and BA) are readily obtained from DFT calculations. However, the inversion symmetry of the 2H bilayer results in band degeneracies. In this case, the layer and spin information that results from a DFT calculation is ambiguous, since any linear combination of degenerate states may be considered a valid eigenstate for that given energy value. We can learn more about the spin and layer polarization of states with degenerate eigenvalues by building simple Hamiltonian models of band edges that respect the system symmetries.

To lay the groundwork for our later discussion, it is important to note that if an operator is a symmetry of a Hamiltonian, then mathematically, the symmetry operator and the system Hamiltonian commute: $\left[\widehat{H}, \hat{S}\right] = 0$. As a consequence of this, the two operators have "simultaneous eigenvectors." That is, if a state is an eigenvector of the Hamiltonian, it will also be an eigenvector of the symmetry operator, written in the proper basis.

MODELING STUDIES

Direct Excitons in WSe_2 Bilayers

Comparing A and B excitons in 2H and 3R

To compare the direct excitons in the 2H and 3R stacked bilayers, we compute a band structure for each stacking type using a PBE DFT calculation as described above. The band structures for the 3R and 2H bilayer are plotted in Figure 3a, b. The consequences of the symmetry differences between the two structures is immediately apparent: the bands for the 3R structure are well layer-polarized at the K point in the Brillouin zone, with bands corresponding to states localized in the upper WSe_2 layer colored blue and bands corresponding to states localized in the lower layer colored magenta. In the BA 3R structure (not shown) the bands look identical but with the upper/lower layer states reversed. In contrast, the 2H structure, which has inversion symmetry, has doubly-degenerate bands across the entire Brillouin Zone. Since the layer-polarization cannot be resolved in DFT, all the doubly degenerate bands are colored black.

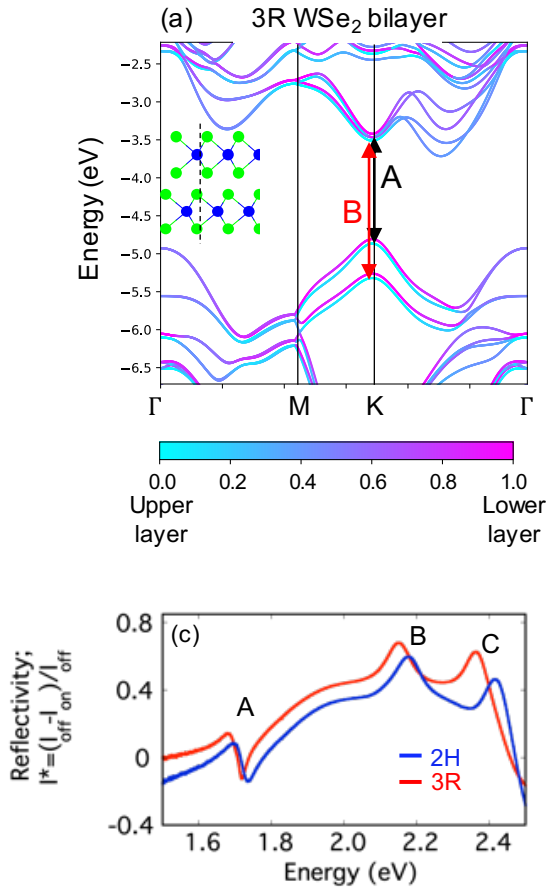

(d)	A (eV)	B (eV)	B – A (meV)	A^{2H}–A^{3R} (meV)	B^{2H}–B^{3R} (meV)
2H (experiment)	1.72	2.18	460	10	30
3R (experiment)	1.71	2.15	440		
2H (theory)	1.402	1.822	420	9	19
3R (theory)	1.393	1.803	410		

Figure 3 – Comparing direct excitons in 3R and 2H structures. Panels (a) and (b) show the DFT-computed band structures of 3R (AB) and 2H bilayers, respectively, with the gaps associated with the A and B excitons marked. Panel (c) shows the differential reflectivity measured for 2H and 3R aligned bilayers at T=4K. Panel (d) compares the DFT-computed and experimentally measured values, showing that DFT captures the higher exciton energy for the 2H A and B excitons measured in experiment. Figure adapted from reference [9].

The band gaps associated with the A and B excitons in each structure are marked with black and red arrows, respectively. An A exciton is composed of an electron and hole from a single layer, so each structure actually contains two A excitons (see detailed schematic in Figure 4). The same is true of the B exciton. The values labeled "A" in the table in Figure 3d are the averaged values for the A excitons in both layers; likewise for the B excitons. These values report the energy difference between the conduction and valence band from which the constituent electron and hole of a given exciton arise.

The true energy of an exciton is the band gap value minus an exciton binding energy, which requires a more complex theoretical treatment to calculate. However, examining the differences in the band gaps for the 3R and 2H structure, we see that we get quite good agreement with experimental differential reflectance measurements (Figure 3c) [9]. This is consistent with the claim that the exciton binding energy is very similar in 2H and 3R structures, and thus cancels out when the difference is taken. Specifically, $\Delta A_{2H-3R} = \left[\left(A_{2H}^{gap} - BE_{2H}\right) - \left(A_{3R}^{gap} - BE_{3R}\right)\right] = \left(A_{2H}^{gap} - A_{3R}^{gap}\right)$ if $BE_{2H} = BE_{3R}$. We then have $\Delta A_{2H-3R}^{DFT} = 9meV$ and $\Delta A_{2H-3R}^{exp} = 10meV$, showing very good agreement. Likewise for the B exciton, $\Delta B_{2H-3R}^{DFT} = 19meV$ and $\Delta B_{2H-3R}^{exp} = 30meV$, also showing good agreement. Thus we see that the DFT calculations capture the higher A and B exciton energies in the 2H structure when compared to the 3R structures, even without considering particle-particle interactions.

Resolving A exciton splitting in 3R bilayers

As described above, the 3R bilayer lacks an inversion center, so the upper- and lower-layer bands are not constrained to be degenerate as in the 2H structure. This does not mean there *must* be splitting in the 3R bands: the bands could have a so-called "accidental" degeneracy. However, in practice, this is not the case. The tungsten atoms in the two layers of a 3R bilayer have a different dielectric environment, seen most clearly in the difference in distance of each tungsten to the nearest selenium atom in the opposite layer. This difference in dielectric environment leads to the observed splitting in the blue and magenta bands at K in the 3R band structure (Fig. 3a).

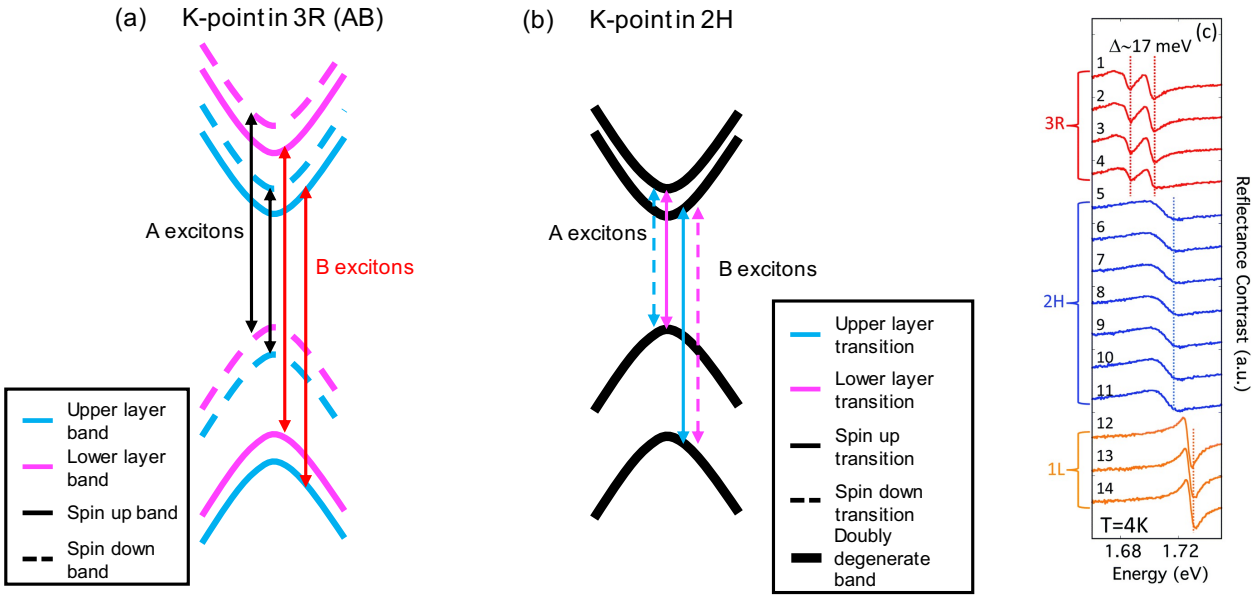

Figure 4 – Exciton splitting in 3R vs 2H. Panels (a) and (b) show a schematic representation of the A and B exciton transitions in 3R and 2H WSe_2 bilayers, respectively. Panel (c) shows reflectance contrast spectra taken on an hBN-encapsulated sample consisting of 3R, 2H, and monolayer WSe_2 regions. The two distinct A exciton energies are apparent in the 3R spectra. Figure adapted from reference [9].

This splitting is exaggerated in the schematic drawing of the excitonic transitions in Figure 4. From this figure, it is clear that there are two A excitons in the 3R bilayer, one from the upper layer, and one from the lower layer, with the lower layer A exciton having a higher energy in the AB bilayer. In the BA structure, the layers are effectively reversed, with the upper layer A exciton having the higher energy, but the difference in A exciton energies remains the same in both cases. The distinct energies of the two excitons are not observed in the reflectance measurement shown in Fig. 3 due to the particular substrate (SiO2/Si), but the distinct exciton energies are observed in measurements taken on an hBN-encapsulated sample, shown in Figure 4c. This data shows reflectance spectra taken at 14 discrete points along a sample that consists of 3R and 2H stacked bilayer, along with monolayer WSe_2 [9]. It is clear that the spectra measured on the 3R portion of the sample exhibit two A exciton dips, while the spectra measured on the 2H and monolayer portions of the sample show only one A exciton dip. The 2H sample has two degenerate A excitons, as shown in Figure 4b, while the monolayer only as one A exciton, as shown in the schematic in Fig. 2. The splitting measured between the A exciton reflectance dips is 17 meV, while the difference between the gaps associated with upper- and lower-layer excitons in the DFT calculations is 12 meV, where we have again assumed the cancellation of the exciton binding energy. The agreement between the DFT

and experimental exciton splitting is again very good, and underscores the utility of these PBE-level DFT calculations for comparing 2D materials with the same chemical makeup, but with different structures.

Indirect Excitons in WSe_2 Bilayers

Indirect excitons in the 3R WSe_2 bilayer

We now turn our attention to the indirect excitons in WSe_2 bilayers. These excitons are bound states of a hole from the top of the valence band at K and an electron from the conduction band minimum at Q, a Brillouin zone point that is on the line between K and Γ. Indirect excitons in bilayer TMDs have longer lifetimes than direct excitons since they tend to be spatially indirect [17] as well as momentum indirect, where the hole is well-localized in one layer, but the electronic weight is distributed over both layers [17, 18]. This diffuse spatial weight of the electron at the conduction band Q point can be seen in the purple color of the conduction band (combination of upper and lower layers) in the 3R band structure shown in Figure 3a. The spin of the electron and hole must also match (or at least have non-zero dot products) in order to result in a bright optical transition.

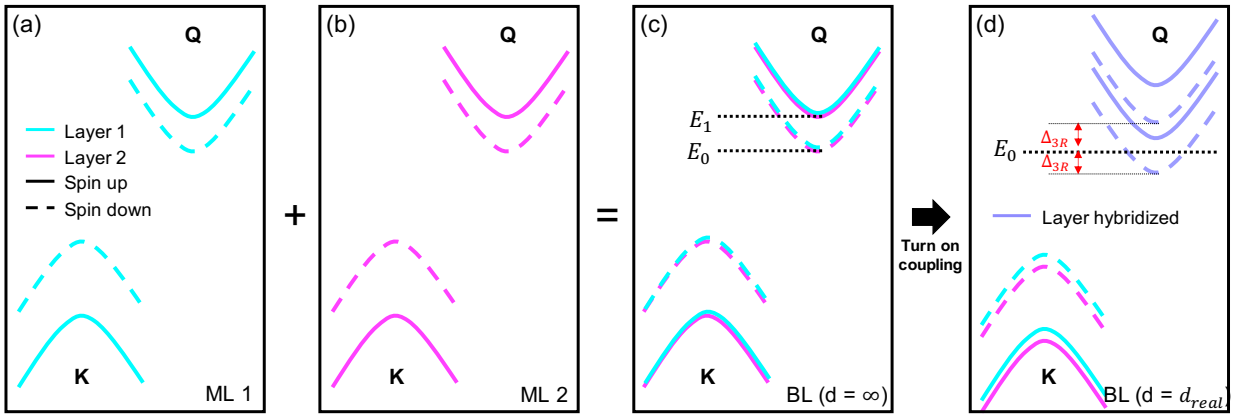

Figure 5 – Bands involved in indirect exciton transitions in 3R bilayers. (a) and (b) show the monolayer bands at K in the valence band and Q in the conduction band. In the 3R stacking, if layers were separated by an infinite distance, the two sets of exactly overlapping bands shown in (c) would result. When coupling is turned on between layers (i.e. real interlayer separation is assumed), the band splitting and hybridization shown in (d) occur. Conduction bands maintain their spin character but become layer-hybridized. The coupling between states in opposite layers but with the same spin is roughly the Δ_{3R} shown in (d).

Because the of the lack of degeneracy in the 3R bands, the spin and layer polarization of bands is readily available from the DFT results. As illustrated in Figure 5, the 3R bilayer bands can be understood as the superposition of the monolayer bands with some interlayer coupling between states in opposite layers but with the same spin. In a rough approximation, the spin-down bands split by $\pm\Delta_{3R}$ around E_0, and the spin-up bands split by $\pm\Delta_{3R}$ around E_1. This is consistent with the energies of the Q-point bands obtained from DFT, with $\Delta_{3R} \cong 0.1$ eV. Given the spin- and layer-matching requirement from the optical selection rules, we see that there are four possible spin-down indirect excitons originating in a given valley in the 3R system: Layer 1 hole with layer-hybridized $E_0 - \Delta_{3R}$ electron, Layer 1 hole with layer-hybridized $E_0 + \Delta_{3R}$ electron, Layer 2 hole with layer-hybridized $E_0 - \Delta_{3R}$ electron, and Layer 2 hole with layer-hybridized $E_0 + \Delta_{3R}$ electron. There are also spin-up excitons in this valley, but they have higher energy, and we focus on the lowest energy indirect excitons here.

Indirect excitons in the 2H WSe_2 bilayer

The layer and spin polarization in the 2H bands are not clear from DFT because the degeneracy of the bands precludes the definition of a unique set of eigenvectors at a given k-point. By analogy with other TMD systems, we know that the valence band maximum states can be considered to be largely spin and layer polarized in this system [16], but the spin and layer polarization in the conduction bands at the Q point is less clear. We will use analytic Hamiltonian analysis to study the Q point conduction band states and to make some comments on the indirect excitons expected in the 2H structure.

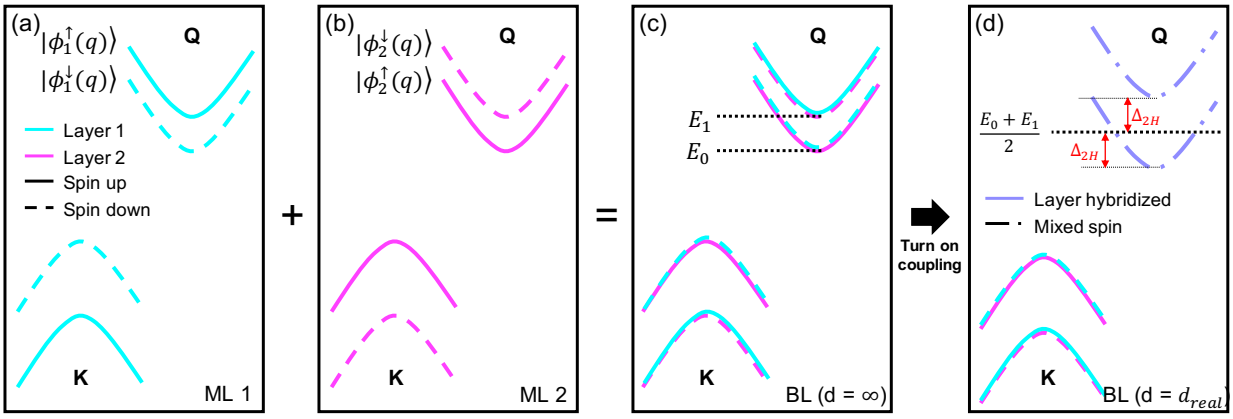

Figure 6 – Bands involved in indirect exciton transitions in 2H bilayers. (a) and (b) show the monolayer bands at K in the valence band and Q in the conduction band. In the 2H stacking, if layers were separated by an infinite distance, the two sets of exactly overlapping bands shown in (c) would result. Note that degenerate bands have opposite spin and layer character, in contrast to the 3R stacking. When coupling is turned on between layers (i.e. real interlayer separation is assumed), the band splitting and hybridization shown in (d) occurs. Conduction bands become both spin-mixed and layer-hybridized.

To begin our analysis, we write the simple energy eigenvalue problem, $H\Psi = E\Psi$, for the four states at the conduction minimum at Q *in each valley: Q and -Q*. We write the states in terms of the monolayer states labelled in Figure 6a, b, and we start in the limit where the layers are infinitely far apart, so the energies are identical to the monolayer band energies (Fig. 6c).

$$\begin{bmatrix} E_0 & 0 & 0 & 0 & 0 & 0 & 0 & 0 \\ 0 & E_0 & 0 & 0 & 0 & 0 & 0 & 0 \\ 0 & 0 & E_0 & 0 & 0 & 0 & 0 & 0 \\ 0 & 0 & 0 & E_0 & 0 & 0 & 0 & 0 \\ 0 & 0 & 0 & 0 & E_1 & 0 & 0 & 0 \\ 0 & 0 & 0 & 0 & 0 & E_1 & 0 & 0 \\ 0 & 0 & 0 & 0 & 0 & 0 & E_1 & 0 \\ 0 & 0 & 0 & 0 & 0 & 0 & 0 & E_1 \end{bmatrix} \begin{bmatrix} |\phi_2^{\uparrow}(q)\rangle \\ |\phi_1^{\downarrow}(q)\rangle \\ |\phi_2^{\downarrow}(-q)\rangle \\ |\phi_1^{\uparrow}(-q)\rangle \\ |\phi_2^{\downarrow}(q)\rangle \\ |\phi_1^{\uparrow}(q)\rangle \\ |\phi_2^{\uparrow}(-q)\rangle \\ |\phi_1^{\downarrow}(-q)\rangle \end{bmatrix} = E \begin{bmatrix} |\phi_2^{\uparrow}(q)\rangle \\ |\phi_1^{\downarrow}(q)\rangle \\ |\phi_2^{\downarrow}(-q)\rangle \\ |\phi_1^{\uparrow}(-q)\rangle \\ |\phi_2^{\downarrow}(q)\rangle \\ |\phi_1^{\uparrow}(q)\rangle \\ |\phi_2^{\uparrow}(-q)\rangle \\ |\phi_1^{\downarrow}(-q)\rangle \end{bmatrix}$$

Now we note that inversion, $\hat{I}$, is a symmetry of the system that negates a position, i.e. $\vec{r} \to -\vec{r}$. The $z \to -z$ change will show up as a change from layer 1 to layer 2, and the $(x, y) \to (-x, -y)$ change will show up as a change in Brillouin zone coordinate $q \to -q$. The inversion operator leaves spin unchanged. Therefore, inversion acting on the monolayer states yields the following:

$$\hat{I}|\phi_1^{\downarrow}(q)\rangle = |\phi_2^{\downarrow}(-q)\rangle$$

$$\hat{I}|\phi_1^{\uparrow}(q)\rangle = |\phi_2^{\uparrow}(-q)\rangle$$

and the inversion operator squares to the identity matrix. We note that the bands at -Q in a given monolayer are identical to the bands at Q, but with a spin-flip. By inspecting panels (a) and (b) in Fig. 6, we can see that the original monolayer state and the inversion-transformed state have the same energy, consistent with the fact that inversion is a symmetry of the 2H Hamiltonian. We can then construct states out of the monolayer energy states that are eigenstates of the inversion operator, and we can write an eigenvalue problem for the inversion operator, $\hat{I}\Psi_I = i\Psi_I$:

$$\begin{bmatrix} 1 & 0 & 0 & 0 & 0 & 0 & 0 & 0 \\ 0 & 1 & 0 & 0 & 0 & 0 & 0 & 0 \\ 0 & 0 & 1 & 0 & 0 & 0 & 0 & 0 \\ 0 & 0 & 0 & 1 & 0 & 0 & 0 & 0 \\ 0 & 0 & 0 & 0 & -1 & 0 & 0 & 0 \\ 0 & 0 & 0 & 0 & 0 & -1 & 0 & 0 \\ 0 & 0 & 0 & 0 & 0 & 0 & -1 & 0 \\ 0 & 0 & 0 & 0 & 0 & 0 & 0 & -1 \end{bmatrix} \begin{bmatrix} |\phi_2^{\downarrow}(-q)\rangle + |\phi_1^{\downarrow}(q)\rangle \\ |\phi_2^{\uparrow}(-q)\rangle + |\phi_1^{\uparrow}(q)\rangle \\ |\phi_2^{\downarrow}(q)\rangle + |\phi_1^{\downarrow}(-q)\rangle \\ |\phi_2^{\uparrow}(q)\rangle + |\phi_1^{\uparrow}(-q)\rangle \\ |\phi_2^{\downarrow}(-q)\rangle - |\phi_1^{\downarrow}(q)\rangle \\ |\phi_2^{\uparrow}(-q)\rangle - |\phi_1^{\uparrow}(q)\rangle \\ |\phi_2^{\downarrow}(q)\rangle - |\phi_1^{\downarrow}(-q)\rangle \\ |\phi_2^{\uparrow}(q)\rangle - |\phi_1^{\uparrow}(-q)\rangle \end{bmatrix} = i \begin{bmatrix} |\phi_2^{\downarrow}(-q)\rangle + |\phi_1^{\downarrow}(q)\rangle \\ |\phi_2^{\uparrow}(-q)\rangle + |\phi_1^{\uparrow}(q)\rangle \\ |\phi_2^{\downarrow}(q)\rangle + |\phi_1^{\downarrow}(-q)\rangle \\ |\phi_2^{\uparrow}(q)\rangle + |\phi_1^{\uparrow}(-q)\rangle \\ |\phi_2^{\downarrow}(-q)\rangle - |\phi_1^{\downarrow}(q)\rangle \\ |\phi_2^{\uparrow}(-q)\rangle - |\phi_1^{\uparrow}(q)\rangle \\ |\phi_2^{\downarrow}(q)\rangle - |\phi_1^{\downarrow}(-q)\rangle \\ |\phi_2^{\uparrow}(q)\rangle - |\phi_1^{\uparrow}(-q)\rangle \end{bmatrix}$$

where i is the inversion eigenvector and not the imaginary unit. We can then construct a matrix U that rotates the energy eigenvector Ψ to the inversion eigenvector Ψ_I: $U\Psi = \Psi_I$, where

$$U = \frac{1}{\sqrt{2}} \begin{bmatrix} 0 & 1 & 1 & 0 & 0 & 0 & 0 & 0 \\ 0 & 0 & 0 & 0 & 0 & 1 & 1 & 0 \\ 0 & 0 & 0 & 0 & 1 & 0 & 0 & 1 \\ 1 & 0 & 0 & 1 & 0 & 0 & 0 & 0 \\ 0 & -1 & 1 & 0 & 0 & 0 & 0 & 0 \\ 0 & 0 & 0 & 0 & 0 & -1 & 1 & 0 \\ 0 & 0 & 0 & 0 & 1 & 0 & 0 & -1 \\ 1 & 0 & 0 & -1 & 0 & 0 & 0 & 0 \end{bmatrix}$$

and is a unitary matrix. U and its inverse $U^{\dagger}$can then be used to write the Hamiltonian in the basis of the inversion eigenstates: $UHU^{\dagger} = H_I$. The 4x4 blocks on the diagonal of H_I correspond to the $i = +1$ and $i = -1$ inversion eigenvalues. Since each entry in the inversion eigenstate also has a well-defined spin, it is now easy to introduce couplings that respect the symmetry and the spin of the system. Introducing couplings here amounts to going from infinitely separated layers to layers with a real separation, as in the transition from panel c to d of Fig. 6. For simplicity, we assume that the coupling strength between spin-up states is the same as that between spin-down states, and we have the following Hamiltonian, written in the inversion basis:

$$H_{Ic} = \begin{bmatrix} E_0 & 0 & \mathrm{t} & 0 & 0 & 0 & 0 & 0 \\ 0 & E_1 & 0 & \mathrm{t} & 0 & 0 & 0 & 0 \\ \mathrm{t} & 0 & E_1 & 0 & 0 & 0 & 0 & 0 \\ 0 & \mathrm{t} & 0 & E_0 & 0 & 0 & 0 & 0 \\ 0 & 0 & 0 & 0 & E_0 & 0 & \mathrm{t} & 0 \\ 0 & 0 & 0 & 0 & 0 & E_1 & 0 & \mathrm{t} \\ 0 & 0 & 0 & 0 & \mathrm{t} & 0 & E_1 & 0 \\ 0 & 0 & 0 & 0 & 0 & \mathrm{t} & 0 & E_0 \end{bmatrix}$$

This matrix has two eigenvalues, $\varepsilon_{\pm} = \frac{1}{2}(E_0 + E_1 \pm \sqrt{E_0^2 - 2E_0E_1 + E_1^2 + 4t^2})$ each of which is four-fold degenerate. This agrees with our DFT calculations, where one Q valley has two doubly degenerate bands, and the degeneracy is doubled if the -Q valley bands are computed. In Figure 6d, $\sqrt{E_0^2 - 2E_0E_1 + E_1^2 + 4t^2}/2$ is denoted Δ_{2H}. Using conduction band edge values from a monolayer DFT calculation (E_0= -3.54861 eV and E_1= -3.32649 eV) along with band edge values from the 2H DFT calculation (ε_+= -3.182434 eV and ε_-= -3.681074 eV), we extract an approximate value of t = 0.2 eV for the coupling between layers at the Q point in the 2H system. This is roughly twice the coupling in the 3R system, where the coupling strength was found from the DFT to be $\Delta_{3R} \cong 0.1$ eV.

Now that we know that our choice of coupling scheme is consistent with the DFT results, we turn to understanding the character of the states at the conduction band Q point. We can construct another unitary matrix U_{HIc}, whose columns are the normalized eigenvectors of H_{Ic}. Beginning with the eigenvalue equation $H_{Ic}\Psi_I = E\Psi_I$, we can rotate by U_{HIc} to obtain

$$U_{HIc}^{\dagger}H_{Ic}U_{HIc}U_{HIc}^{\dagger}\Psi_I = EU_{HIc}^{\dagger}\Psi_I$$
$$H_{Ec}\Psi_{Ec} = E\Psi_{Ec}$$

where the subscript "Ec" indicates that we are back in the energy basis, this time with the coupling included. Ψ_{Ec} in particular will tell us the spin and layer character of the bands at the conduction band minimum at the Q point. To make things even clearer, we will swap the third and fourth elements with the fifth and sixth elements, which amounts to a rotation into the "valley basis," where each 4x4 diagonal block of the Hamiltonian will correspond to the energies in one valley. (i.e. The diagonal of H in the valley basis will read E_0, E_0, E_1, E_1, E_0, E_0, E_1, E_1, rather than E_0, E_0, E_0, E_0, E_1, E_1, E_1, E_1, as in the energy basis.) Since we are only concerned with layer and spin, we drop the q/-q notation in the vector for clarity's sake, and adopt a notation indicating only $|layer\#, spin\rangle$:

$$\Psi_{Ec}^{Valley} = \begin{bmatrix} \alpha(|1,\uparrow\rangle - |2,\uparrow\rangle) - \beta(|1,\uparrow\rangle + |2,\uparrow\rangle) \\ -\alpha(|1,\downarrow\rangle + |2,\downarrow\rangle) + \beta(|1,\downarrow\rangle - |2,\downarrow\rangle) \\ -\alpha(|1,\uparrow\rangle - |2,\uparrow\rangle) - \beta(|1,\uparrow\rangle - |2,\uparrow\rangle) \\ -\alpha(|1,\downarrow\rangle - |2,\downarrow\rangle) - \beta(|1,\downarrow\rangle - |2,\downarrow\rangle) \\ -\alpha(|1,\uparrow\rangle + |2,\uparrow\rangle) + \beta(|1,\uparrow\rangle + |2,\uparrow\rangle) \\ \alpha(|1,\downarrow\rangle + |2,\downarrow\rangle) - \beta(|1,\downarrow\rangle + |2,\downarrow\rangle) \\ \alpha(|1,\uparrow\rangle + |2,\uparrow\rangle) + \beta(|1,\uparrow\rangle + |2,\uparrow\rangle) \\ \alpha(|1,\downarrow\rangle + |2,\downarrow\rangle) + \beta(|1,\downarrow\rangle + |2,\downarrow\rangle) \end{bmatrix}$$

where α, β are constants dependent on E_0, E_1, and t. With DFT values for E_0 and E_1 and t = 0.2 eV, they take the values of $\alpha = 0.507212$ and $\beta = 0.861821$. The two valleys (top four and bottom four entries) look different here, because in truth the q/-q label matters. However, for our purposes, the two valleys look *the same* in that each energy band corresponds to two states: one with spin-up layer-mixed states, and one with spin-down layer-mixed states. This is illustrated in Fig. 6d as purple dash-dot bands.

As discussed previously, the allowed optical transitions in TMDs must originate from bands which have overlap in spin and layer [5]. Thus, there are also four possible interlayer excitons in the 2H WSe_2 bilayer, but only *two* distinct energies. The low-energy indirect exciton in the 2H system can comprise the spin-down hole in layer 1 and the spin-mixed, layer-mixed electron at $(E_0 + E_1)/2 - \Delta_{2H}$ or the spin-up hole in layer 2 and the spin-mixed, layer-mixed electron at $(E_0 + E_1)/2 - \Delta_{2H}$. The higher-energy indirect exciton in the 2H system can involve the spin-down hole in layer 1 and the spin-mixed, layer-mixed electron at $(E_0 + E_1)/2 + \Delta_{2H}$ or the spin-up hole in layer 2 and the spin-mixed, layer-mixed electron at $(E_0 + E_1)/2 + \Delta_{2H}$. It is possible that careful experiments could resolve the difference between

the two distinct indirect excitonic energies in the 2H system and the four distinct indirect excitonic energies of the 3R system.

CONCLUSIONS

The modeling studies detailed in this report show that Density Functional Theory calculations at the PBE level and analytic Hamiltonian models are fruitful methods for studying the excitonic physics in transition metal dichalcogenide bilayers. As we continue to better understand the exciton structure of 2D materials such as WSe_2, we increase our ability to harness the remarkable optical and electronic properties of these materials for naval applications, particularly for sensing technologies and next-generation low-power and light-weight electronics.

Our DFT results on WSe_2 bilayers agree well with experimental reflectance studies, capturing the higher energies of the A and B excitons in 2H when compared to 3R samples. Furthermore, the DFT predicts the two distinct A exciton peaks seen in hBN-encapsulated 3R samples, which arise from slightly differing contributions from each layer. Meanwhile, the analytic Hamiltonian studies provide information about layer and spin character of states that can be hard to obtain from DFT calculations on systems with inversion symmetry, such as the 2H bilayer. The agreement between energies computed with the analytic models and the DFT results suggests that the analytic model results are useful for comparing to experiment, just as the DFT results have proven to be. The analytic model predicts an interlayer coupling at the conduction band Q point that is twice as strong in the 2H as in the 3R system. It also predicts two discrete energies for indirect K to Q excitons in the 2H structure, whereas the 3R structure is expected to exhibit four discrete low-energy indirect exciton peaks. Collaborations with experimental groups at NRL are ongoing to test these results and continue to map the intricacies of 2D materials.

REFERENCES

1. K.S. Novoselov, A.K. Geim, S.V. Morozov, D. Jiang, Y. Zhang, S.V. Dubonos, I.V. Grigorieva, A.A. Firsov, 2004, “Electric Field Effect in Atomically Thin Carbon Films,” Science 306(5696), 666-669. doi: 10.1126/science.1102896.

2. K.S. Novoselov, A. Mishchenko, A. Carvalho, A.H. Castro Neto, 2016, “2D materials and van der Waals heterostructures,” Science 353(6298). doi: 10.1126/science.aac9439.

3. B. Huang, G. Clark, E. Navarro-Moratalla, D.R. Klein, R. Cheng, K.L. Seyler, D. Zhong, E. Schmidgall, M.A. McGuire, D.H. Cobden, W. Yao, D. Xiao, P. Jarillo-Herrero, X. Xu, 2017, “Layer-dependent ferromagnetism in a van der Waals crystal down to the monolayer limit,” Nature 546, 270-273. doi: 10.1038/nature22391.

4. K. Khan, A.K. Tareen, M. Aslam, R. Wang, Y. Zhang, A. Mahmood, Z. Quyang, H. Zhang, Z. Guo, 2020, “Recent developments in emerging two-dimensional materials and their applications,” Journal of Materials Chemistry C 8, 387-440. doi: 10.1039/C9TC04187G.

5. T. Mueller and E. Malic, 2018, “Exciton physics and device application of two-dimensional transition metal dichalcogenide semiconductors,” npj 2D Materials and Applications 2, 29. doi: 10.1038/s41699-018-0074-2.

6. S. Brem, A. Ekman, D. Christiansen, F. Katsch, M. Selig, C. Roberg, X. Marie, B. Urbaszek, A. Knorr, E. Malic, 2020, “Phonon-assisted photoluminescence from indirect excitons in monolayers of

transition-metal dichalcogenides," Nano Letters 20(4), 2849-2856. doi: 10.1021/acs.nanolett.0c00633.

7. Y. Cao, V. Fatemi, S. Fang, K. Watanabe, T. Taniguchi, E. Kaxiras, P. Jarillo-Herrero, 2018, "Unconventional superconductivity in magic-angle graphene superlattices," Nature 556, 43-50. doi: 10.1038/nature26160.

8. Y. Yang, J. Li, J. Yin, S. Xu, C. Mullan, T. Taniguchi, K. Watanabe, A.K. Geim, K.S. Novoselov, A. Mishchenko, 2020, "In situ manipulation of van der Waals heterostructures for twistronics," Science Advances 6(49). doi: 10.1126/sciadv.abd3655.

9. K.M. McCreary, M. Phillips, H.-J. Chuang, D. Wickramaratne, M. Rosenberger, C.S. Hellberg, B.T. Jonker, 2022, "Stacking-dependent optical properties in bilayer WSe2," Nanoscale 14(1), 147-156. doi: 10.1039/D1NR06119D.

10. J.P. Perdew, K. Burke, M. Ernzerhof, 1996, "Generalized gradient approximation made simple," Physical Review Letters 77(18), 3865-3868. doi: 10.1103/PhysRevLett.77.3865.

11. P.E. Blöchl, 1994, "Projector augmented-wave method," Physical Review B 50(24), 17953-17979. doi: 10.1103/PhysRevB.50.17953.

12. G. Kresse, D. Joubert, 1999, "From ultrasoft pseudopotentials to the projector augmented-wave method," Physical Review B 59(3) 1758-1775. doi: 10.1103/PhysRevB.59.1758.

13. G. Kresse, J. Furthmüller, 1996, "Efficient iterative schemes for *ab initio* total-energy calculations using a plane-wave basis set," Physical Review B 54(16), 11169-11186. doi: 10.1103/PhysRevB.54.11169.

14. S. Grimme, J. Antony, S. Ehrlich, H. Krieg, 2010, "A consistent and accurate ab initio parametrization of density functional dispersion correction (DFT-D) for the 94 elements H-Pu," The Journal of Chemical Physics 132(15), 154104. doi: 10.1063/1.3382344.

15. J. Kang, S. Tongay, J. Zhou, J. Li, J. Wu, 2013, "Band offsets and heterostructures of two-dimensional semiconductors," Applied Physics Letters 102(1), 012111. doi: 10.1063/1.4774090.

16. M. Phillips, C.S. Hellberg, 2019, "Commensurate structures in twisted transition metal dichalcogenide heterobilayers," arXiv:1909.02495v2.

17. Y. Jiang, S. Chen, W. Zheng, B. Zheng, A. Pan, 2021, "Interlayer exciton formation, relaxation, and transport in TMD van der Waals heterostructures," Light: Science & Applications 10, 72. doi: 10.1038/s41377-021-00500-1.

18. A.T. Hanbicki, H.-J. Chuang, M.R. Rosenberger, C.S. Hellberg, S.V. Sivaram, K.M. McCreary, I.I. Mazin, B.T. Jonker, 2018, "Double indirect interlayer exciton in a $MoSe_2/WSe_2$ van der Waals heterostructure," ACS Nano 12(5), 4719-4726. doi: 10.1021/acsnano.8b01369.